International Communications in Heat and Mass Transfer 140 (2023) 106496

Contents lists available at ScienceDirect

International Communications in Heat and Mass Transfer

journal homepage: www.elsevier.com/locate/ichmt

Experimental study on the heat transfer performance of a vapour chamber with porous wick structures printed via metallic additive manufacturing

Xu Meng [a,b], Shujie Tan [c], Zhipeng Yuan [a,b], Yicha Zhang [d,1,**], Liheng Chen [a,e,*,1]

[a] Changchun Institute of Optics, Fine Mechanics and Physics (CIOMP), Chinese Academy of Science, Changchun 130033, China
[b] University of Chinese Academy of Sciences, Beijing 100049, China
[c] College of Mechanical and Electrical Engineering, Nanjing University of Aeronautics and Astronautics, Nanjing 210016, China
[d] ICB-COMM, UMR 6303, CNRS, Université Bourgogne Franche-Comté, UTBM, Belfort, France
[e] Centre of Materials Science and Optoelectronic Engineering, University of Chinese Academy of Science, Beijing 100049, China

ARTICLE INFO

Keywords:
Parametric porous wick
Heat transfer performance
Vapour chamber
Additive manufacturing
Thermal resistance

ABSTRACT

Two types of vapour chamber with integrated three-dimensionally (3D) printed wicks, namely a single-pore 3D printed wick vapour chamber and hybrid-pore 3D printed wick vapour chamber, were designed, printed, and tested to demonstrate the feasibility of constructing VCs through metallic additive manufacturing. A water-cooling test system was established to study the temperature distribution, thermal resistance, and maximum heat transfer power of the VCs. The effects of the cooling-water temperature, heat source area, and hybrid-pore wick structure on the heat transfer performance of the VCs were explored. The results show that the vapour chamber with a 3D printed wick had efficient heat transfer in the range of 0–100 W. The cooling-water temperature greatly affected the heat transfer performance of the VCs. The 3D printed hybrid-pore wick improved the temperature uniformity and heat transfer of the VC. When $P = 100$ W, the thermal resistance of the hybrid-pore 3D printed wick vapour chamber was 0.077 °C/W at a cooling-water temperature $T_w = 40$ °C. The test results indicate that the application of Additive Manufacturing (AM) in fabricating high-performance VCs is feasible and provides more freedom in terms of customizing the heat transfer performance and integrating with the structural design of the heat source.

1. Introduction

The vapour chamber (VC) is a high-efficiency heat conduction device similar to a flat heat pipe [1]. The VC mainly comprises a vacuum cavity, a wick, and working fluid, and it completes the heat transfer through the phase change of the working fluid in the capillary wick. The VC has low heat transfer resistance owing to its larger heat exchange area and shorter phase change loop path. The VC has been widely used in the cooling of high-power devices, such as light-emitting diodes, central processing units, graphical processing units, and high-speed hard drives [2–4]. The wick structure greatly affects the heat transfer performance of the VC. It provides the capillary force for the circulation of the working fluid and the circulation channel for the VC, thereby maintaining the phase change heat dissipation cycle of the working fluid inside the VC [5]. However, existing methods of manufacturing wicks face difficulties in forming parametric and complex porous structures, the pores are formed in a random way during sintering and the sintered structures cannot be controlled and usually have many blinded pores or fine channels that result in a fluid circulation problem. In the grooving manufacturing method, the complexity of internal pores or grooves is limited to the accuracy of tooling devices, which usually form only relatively simple shapes that restrict the functional performance.

To solve the above problem, additive manufacturing (AM) has been identified as a promising candidate technology for fabricating controllable parametric porous structures for the wicks. AM is well suited to the fabrication of complex structures with a relatively low lifecycle cost and enables part consolidation with integrated printing [6]. This advantage had been widely demonstrated for different applications where internal channels and freeform surface structures exist [6,7]. More recently, adopting an advanced design and printing strategy, an AM process,

* Corresponding author at: Changchun Institute of Optics, Fine Mechanics and Physics (CIOMP), Chinese Academy of Science, Changchun 130033, China.
** Corresponding author.
E-mail address: chenliheng3@163.com (L. Chen).
[1] Yicha Zhang and Professor Liheng Chen have made the same contribution.

https://doi.org/10.1016/j.icheatmasstransfer.2022.106496

Available online 25 November 2022

selective laser melting, was shown to be able to print parametric complex fine porous structures with a pore size of <200 μm under stable control and form complex and fine internal channels [8]. Inspired by this work, the present paper investigates the feasibility of using AM to print integrated porous wick structures for the application of a VC. Two types of VC with hybrid parametric porous wicks are designed and printed. A set of heat transfer experiments are then conducted to characterize the functional performances of the VCs. The experimental investigation suggests strong application potential.

The remainder of the paper is organized as follows. Section 2 gives a brief review of representative works on wick design and manufacturing. Section 3 introduces the design and printing of the two types of VC. Section 4 presents details about the experiment and a thorough technical discussion and Section 5 concludes the work by presenting perspectives on future research.

2. Related works on wick design and manufacturing

Traditionally manufactured capillary wicks mainly include the sintered powder wick, wire mesh sintered wick, and grooved wick [9]. Chen et al. [10] studied the effect of the liquid filling rate and leakage on the heat transfer performance of an AI 6061 flat plate heat pipe (FPHP). The experimental results indicate that inappropriate vacuum and leakage diminish the heat transfer performance of FPHPs and the thermal resistance to a minimum of 0.254 °C/W at a filling rate of 25%. Wong et al. [11] conceived a VC with a sintered porous structure in the evaporation wick and a grooved structure in the condensation wick. On the heat transfer performance of the vapour chamber, the impacts of working fluids such as water, methanol, and acetone were examined. The results indicate that water has the highest maximal heat load, whereas acetone has the lowest. The minimum thermal resistance of VC is 0.14 °C/W when the heating output is 120 W. Liu et al. [12] developed a circular VC with a vein-like fractal network wick by simulating the transport of plant leaf water, the condenser wick was made by chemical etching and mechanical engraving respectively. The fractal angle of the vein-like fractal network affected the circulation of the liquid inside the VC, the thermal resistance of the VC dropped as the heat flow increased, and the minimum thermal resistance was 0.06 °C /W at 90 W/cm2. Huang et al. [13] produced a multi-layer sintered mesh wick VC and studied the effects of the number of coarse meshes and wire diameter, the number of fine meshes, the angle of inclination, and the temperature of the cooling water on the heat transfer performance of the ultra-thin VC. They discovered that the heat resistance of UTVCs declined as the coarse mesh count fell, but increased when the wire diameter increased. When the heating power was 50 W, the heat transfer resistance of the 1.53-mm VC was 0.197 °C/W, which was approximately 4.4 times lower than that of a 1.5-mm copper plate. Lefèvre et al. [14] proposed two types of FPHP with different wick structures, namely a sintered mesh and mesh groove structure. Studies have shown that the hybrid wick structure effectively enhances the working performance of a FPHP in an oblique direction. Oshman et al. [15] manufactured a flat, flexible, and lightweight polymer FPHP utilizing a low-cost film composed of low-density polyethylene terephthalate, aluminum, and polyethylene layers for the shell. As the wick structure, a three-layer sintered copper mesh was utilized, while water served as the working fluid. Experiments examine the heat transmission performance of the FPHP at 0°, 45°, and 90° of flexion. When the heating power was 25 W, their results indicated that the heat transfer resistance was roughly 1.1 °C/W. Chen et al. [16] produced two types of 6061 aluminum alloy VC, one with a radial groove wick and the other with a sintered aluminum powder wick. The dimensions of the VCs were 58 mm × 58 mm × 6 mm, and the working fluid was acetone. They found that the VC with a sintered wick had lower heat transfer resistance. Tang et al. [17] embedded copper pillars of sintered copper powder in VCs as a liquid flow path to improve the heat transfer performance of the VCs. In this vapour chamber, the wick structure is comprised of sintered copper powder layers on the top and bottom plates, which serve as the evaporator and condenser wicks, respectively, and sintered copper powder rings embedded with solid copper columns, which serve as the liquid flow channel. Copper powder rings make direct contact with the tips of the condenser and evaporator wicks to create a short path for the working fluid to return. Copper columns are welded to the top and bottom plate to prevent the deformation of the vapour chamber induced by the pressure difference between the interior and exterior. The manufactured VCs had thickness of 3 mm, and a minimum thermal resistance of 0.04 °C/W when the thermal load was 300 W. Kim et al. [18] built unit cell models employing monolayer SEM images and the minimal surface energy principles, and the point-wise thermal-hydraulic equations were solved to determine the monolayer parameters as a function of retreating meniscus. He et al. [19] used photolithography and deep reactive ion etching to create a silicon VC, and an electron beam deposition and lift-off method was used to fabricate a platinum heater and four resistance thermometers. Their experimental results showed that under the condition of 15 °C superheating and heat flux of 15 W/cm2, the silicon VC had excellent performance on an uncharged control sample.

As outlined above, there has been much study of the traditional manufacturing of wicks and the heat transfer performance of VCs produced in traditional manufacturing. Studies have shown that the capillary wick structure is the main factor affecting the heat transfer performance of the VC, and the heat transfer performance of the VC can be improved by combining different structure types or different pore sizes to form a hybrid wick structure. However, existing traditional wick processing methods face problems such as complex procedures, an inability to accurately control the size of the aperture of each part of the wick, difficulty in manufacturing special-shaped capillary wicks, and an inability to integrated manufacturing of VCs [21–23]. These problems greatly limit efforts to improve the heat transfer performance of the VC and the miniaturization and integration of the VC. As discussed in Section 1, in recent years, the rapid development of metal AM technology has enabled the three-dimensional printing of fine metal structures [24–26]. It is possible to realize the integrated manufacturing of the VC and its structural parts. This paper thus reports on the design and manufacture of a single pore and hybrid pore 3D printed wick with porous structure support columns. A frame structure, triply periodic minimal surface (TPMS) gyroid structure, and TPMS Schwarz P structure are used at the three positions of the evaporation wick, condensation wick, and porous structure column, respectively. By planning the printing path and adjusting the printing parameters, the three-dimensional-printing integrated manufacturing of a porous structure of different structure types and different cell sizes for each part of the wick is realized. Two VCs integrating 3D printed wicks are obtained through liquid filling and packaging to study the effect of the three-dimensionally (3D) printed wick structure, heating power, heat source size, and composite aperture wick on the heat transfer performance of the VC and to explore the possibility of the integrated manufacturing of VCs. The next section presents details of the wick printing and manufacturing of VCs.

3. Materials and methods

3.1. Wick design and 3D printing

In this research, we split the wick structure into three functional modules based on the working principle of the vapour chamber: the condensing wick, the porous structure support column, and the evaporation wick. In accordance with the distinct functions of each functional module in the phase change heat transfer cycle of the working fluid within the vapour chamber, different types of porous structures were employed in each functional module. The TPMS-Gyroid structure is utilized in the condenser wick due to its bigger specific surface area, which can provide a greater heat exchange area for the exothermic condensation of steam. The TPMS Schwarz P structure has a vertical

flow channel that is straight. Using it in the center porous support column can create a low-resistance, rapid-return channel for the working liquid to move from the condensation end to the evaporation end. This will accelerate the fluid's circulation within the vapour chamber. The frame porous structure is utilized at the evaporation wick because the printing and control molding technologies of the frame structure are the most developed in the current 3D printing technology of fine porous structure. By adjusting the printing conditions, the frame structure wick's pore size can be reduced while its porosity is maintained. Consequently, the evaporation wick of the frame construction will have a big capillary suction force, a large permeability, and a large porosity, enhancing the heat transfer performance of the vapour chamber.

As shown in Fig. 1, the capillary wick mainly comprised the evaporation wick, the condensation wick, and the support column of the porous structure. The wick of the VC was integrally printed through selective laser melting AM. Two wicks were printed, namely a single-pore wick and a hybrid-pore wick. In the case of the single-pore wick, the evaporation wick adopts a frame porous structure with a cell size of 240 μm [27], the porous structure support column adopts a TPMS Schwarz-P structure with a cell size of 600 μm, and the condensing wick adopts a TPMS gyroid structure with a cell size of 900 μm [8]. The frame-type porous structure with a small cell size in the evaporation wick provides greater capillary pressure and accelerates the circulation of the liquid in the VC. The large-cell-size structure used in the condensation wick and the porous structure column has excellent permeability that reduces the resistance of the liquid backflow. The hybrid-pore wick is based on the single-pore wick and realized by adding a 15 mm × 15 mm small-pore porous structure with a cell size of 160 μm at the centre of the evaporation wick. The small-pore porous structure at the centre of the evaporator wick provides higher capillary pressure for liquid circulation and further improves the heat transfer performance of the VC. (See Tables 1 and 2.)

Each wick was 3D printed and manufactured using copper powder and a selective laser sintering process. A commercial printer (Ti150 3D printer) was used for printing. The three-dimensional printing of the wicks had three main steps: pre-processing, printing, and post-processing. Preprocessing involved generating a laser scanning trajectory file in a self-made trajectory plan script. Printing of the wicks was carried out using copper powder (Zhejiang Yatong soldering material CuSn10) and Ti150 equipment (China Profeta) as shown in Fig. 2. Table 3 lists the printing parameters. Post-treatment involved annealing the wicks in a heat treatment furnace as follows. Samples were kept at a temperature of 820 °C for 2 h and cooled in the furnace to eliminate residual stress. After heat treatment, use wire cutting to cut from the disc sample. Sandblasting and an airflow were adopted to clean residual powder from the porous structure. The final wicks were obtained after 30 min of ultrasonic cleaning. (See Table 4.)

Two 3D printed wicks were characterized using a measurement tool digital microscope system (RH-2000, Hirox, Japan), The OM images are shown in Fig. 3. The OM image reveals the adhesion of powder in the pores of the small-cell-frame porous structure in the evaporation part of the hybrid-pore wick and shows that the porous structures of other wick structures are well formed.

The effective pore diameters of the 3D printed wicks were measured using the pressurised bubbling method [28]; air was injected into the closed cavity holding the test piece by the air pump, and the lower end of the test piece was immersed in the liquid. The pressure was increased until bubbles appeared in the liquid, and the gas pressure P in the closed cavity was measured using a pressure gauge. As the surface tension σ of the liquid was known, the effective capillary pore diameter r_{eff} of the wick was obtained as:

$$r_{eff} = \frac{2\sigma}{P} \tag{1}$$

During pressurisation, the air flow was evenly injected; the bubbling pressure P was measured when the first bubble appeared in the camera record. The surface tension of the liquid at room temperature (24 °C) was obtained from a table ($\sigma = 72.1$ mN/m).

The experimental results shown that: in the evaporation wick, the effective pore diameter r_{eff} of the frame structure with a large cell size is approximately 92 μm whereas that with a small cell size is approximately 39 μm.

In this work, the porosity of the 3D printed wicks is calculated using an analytical balance to measure the weight of the 3D printed wick test piece before and after it filling with water. The mass of the container and liquid mass (M_1) were measured before the test piece was immersed in the liquid. After one end of the test piece was immersed in the liquid and the liquid filled the internal voids of the capillary wick through capillary action, the total mass of the container and liquid (M_2) was measured. The total volume of the test piece (V) was calculated using the manufacturing dimensions of the test piece. The density of the liquid (ρ) was known; thus, the porosity of the porous structure (ε) was obtained using Eq. (2):

$$\varepsilon = \frac{M_1 - M_2}{\rho V} \times 100\% \tag{2}$$

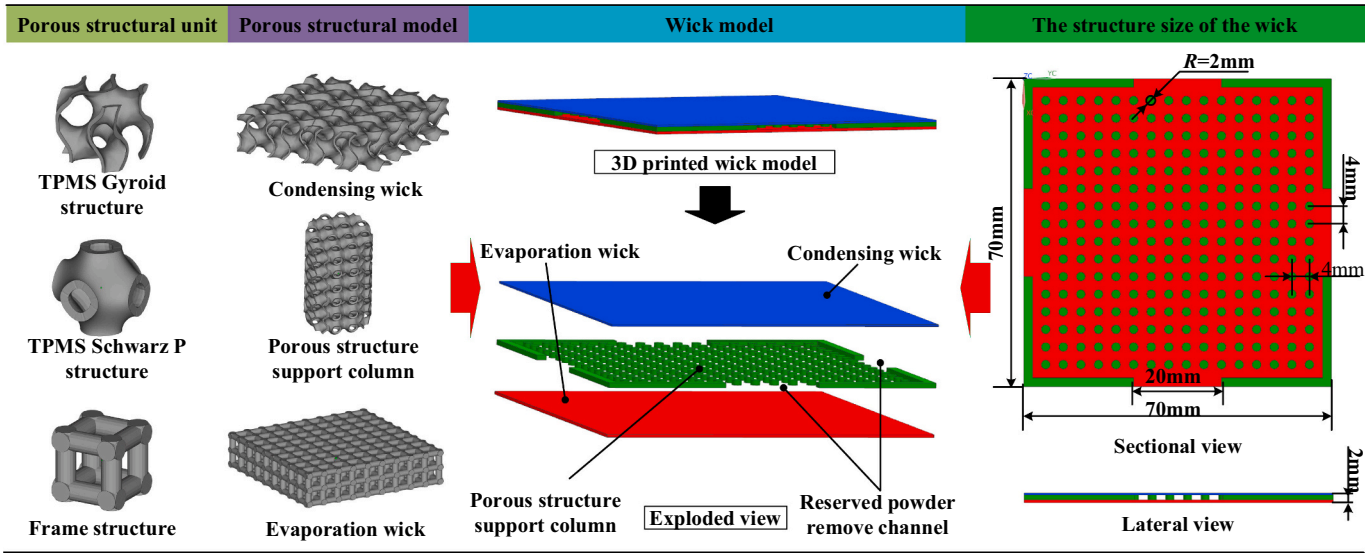

Fig. 1. Schematic diagram of 3D printing wick structure.

Table 1
Summary of conventional VCs in the literature.

Ref.	A_{vc} mm^2	A_h mm^2	t mm	Wick	Working fluid	ε	Q_{max} W	R_{min} °C /W
[10]	150 × 50	50 × 30	2.5	Groove (extrusion process)	Acetone	25%	47	0.254
[11]	100 × 90	31 × 31	1–1.5	Mesh sintered & Groove	Water, Acetone, Methanol		120	0.14
[12]	3846	10/20/30	2	Groove	Water		90	0.06
[13]	100 × 65	20 × 20	1.26–1.77	Mesh sintered (multilayer)	Water	100%	50	0.197
[14]	267 × 115	55.1 × 96.5	1.5	Mesh sintered & Groove	Methanol		40	0.24
[15]	130 × 170	25 × 25	1.31	Copper Mesh & Nylon Mesh	Water		30	1.2
[16]	62 × 62	13.9 × 13.9	6	Sintered aluminum powder	Acetone	55%	80	0.69
[17]	90 × 90	10 × 10	3	Sintered powder	Water		300	0.08
[19]	30 × 30	10 × 10	0.017	Photolithograph & Deep etching	Water		38	1.6

Table 2
The structure size of 3D printing wick structure.

Wick structure of VC	Structure size (mm)
Condensing wick	70 × 70 × 0.4
Evaporation wick	70 × 70 × 0.6
Steam chamber	70 × 70 × 1
Porous structure support column	Φ2 × 1
Spacing between porous structure columns	4

The experimental results show that: the overall porosity of the single-pore wick was 61% whereas that of the hybrid-pore wick was 54%.

3.2. Filling and packaging of the VCs

The filling of the VCs involved a series of steps. The first step was the sandblasting and ultrasonic cleaning of the 3D printed wick to remove the residual powder inside the wick structure and the remaining impurities on the surface. The second step was to manufacture the VC copper shell. The thickness of the prefabricated VC shell was 0.5 mm, as shown in Fig. 4. The third step was to place the printed wick in the prefabricated evaporation copper shell, cover the prefabricated condensing shell, install the liquid filling tube, and place it in the diffusion soldering furnace for welding. During the high-temperature diffusion welding process, pressure was applied between the upper and lower sides of the VCs to ensure the wick and shell tightly bonded. The fourth step was filling the VCs with liquid and sealing the liquid filling tube. Following 30 min of ultrasonic cleaning, degassing, and filling with a certain amount of deionized water, secondary degassing, the exhaust tube was sealed and welded. Finally, CNC finishing was applied to the outer wall of the VCs to complete the manufacturing. The two manufactured VCs, namely the single-pore 3D printed wick vapour chamber (AMVC) and hybrid-pore 3D printed wick vapour chamber (AMVC-H), are shown in Fig. 5.

The working fluid filling rate in the VCs was about 90%, and it was obtained as:

$$\eta = \frac{V_{wl}}{V_{por}} \tag{3}$$

where is the volume of deionized water charging in the VCs.

4. Experimental method

4.1. Experimental test system

The system for testing the heat transfer performance of the VCs is shown in Fig. 6. The system includes four parts: a heating module, water-cooled heat dissipation module, temperature data acquisition module, and thermal insulation boundary. Two ceramic heating blocks with different heating areas are used as the heat source, and the loading power of the heating block is provided by a direct-current (DC) power

Table 3
Constant parameters during the printing of the VC wick structure.

Print Parameter	VC wick structure
Material	Copper powder (CuSn10)
Powder particle size (μm)	15–53
Layer thickness (mm)	0.03
Spot compensation (mm)	0.05
Contour number	1
Contour laser power (W)	75
Contour laser speed (mm/s)	2800

Table 4
The parameters of the manufactured uniform Vapour Chamber.

VC	VC structure size (L × W × t)(mm)	Hybrid wick size (L × W)(mm)	Filling ratio η (%)
AMVC	77.5 × 77.7 × 2.97		90
AMVC-H	77.6 × 77.5 × 2.96	15 × 15	90

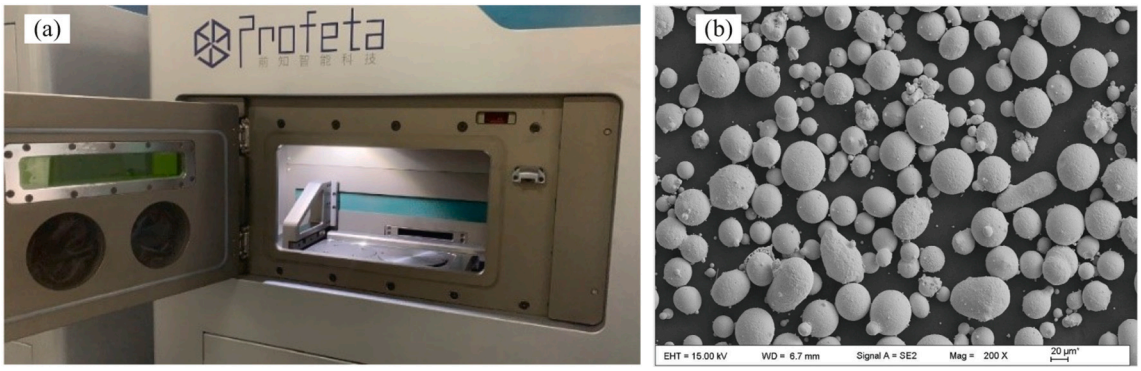

Fig. 2. (a)Ti150 machine (b) Scanning electron microscope image of copper powder.

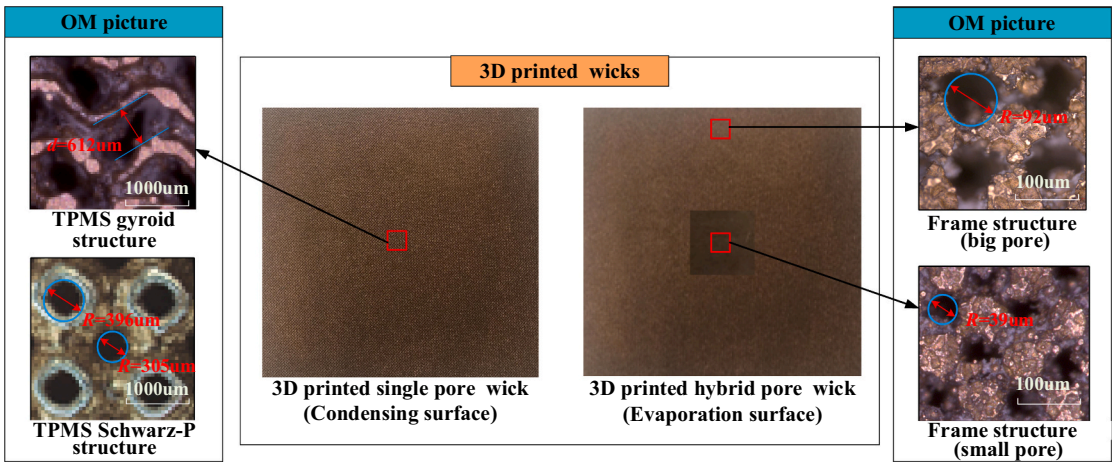

Fig. 3. 3D printing wicks and OM images of each area.

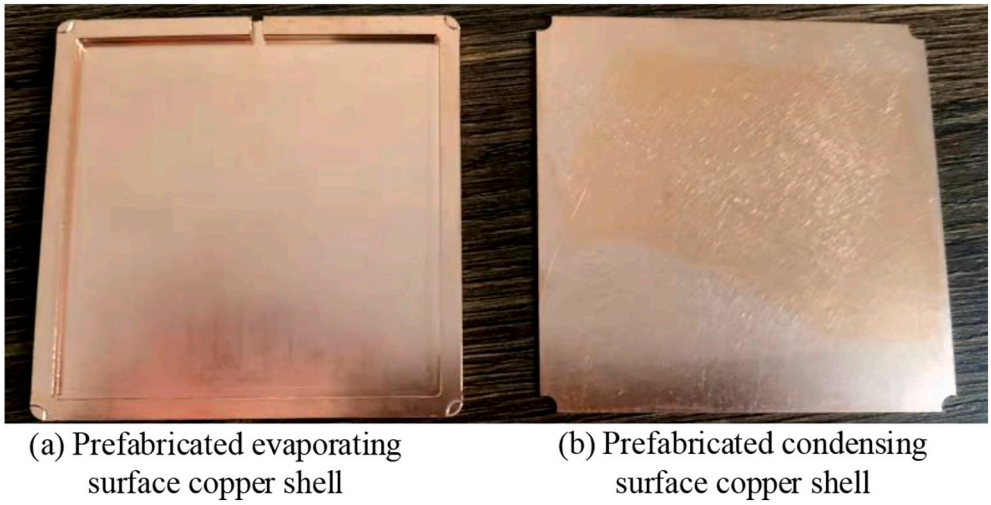

Fig. 4. Prefabricated VC copper shell.

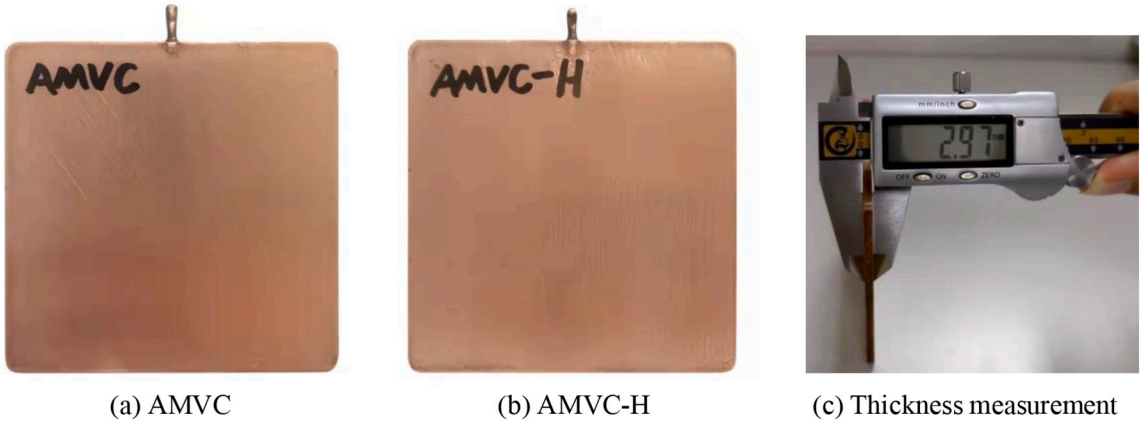

Fig. 5. Manufactured vapour chambers.

supply. The water-cooled heat dissipation module includes a stainless-steel water-cooling plate and a cooling-water circulation system. The temperature data acquisition module uses 14 thermocouples and a computer to collect and store temperature data. The outer diameter of the thermocouple is 0.23 mm. The adiabatic boundary comprises Bakelite (thermal conductivity <0.3 W/(m·K)) and insulation cotton (thermal conductivity <0.05 W/(m·K)) to thermally isolate the experimental system and external environment and improve the accuracy of the experimental results [29,30]. Through the finite element thermal simulation calculation, it is obtained that 95% of the heat of the heat source passes through the VC and finally dissipates through the water-cooling plate. In the experiment, the heating block's loading power

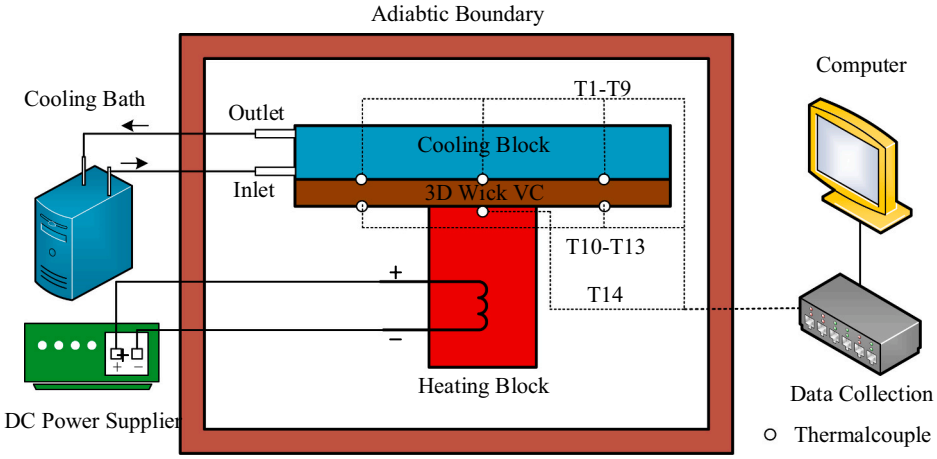

Fig. 6. Schematic diagram of the test system for the heat transfer performance of the VC.

exceeds the heat source's setting power value, which includes the heat loss component. The following describes the link between the loading power of the heating block and the setting heat source power:

$$P = P_{DC} \times (1 - 5\%) \tag{4}$$

Where, P is the setting heat source power, and P_{DC} is the loading power of the heating block.

The layout of the thermocouples in the test system is shown in Fig. 7. Thermocouples T1–T9 are arranged on the condensing surface, T10–T13 are arranged on the evaporation surface, and T14 is arranged on the top surface of the heating block. Multiple predictions were performed before the experiment to ensure the accuracy of the thermocouple temperature measurements. (See Fig. 8.)

In the experiment, the VC was placed horizontally. To ensure good heat transfer between the VC, heating block, and water-cooled plate, the two contact surfaces were coated with thermally conductive silicone grease (having thermal conductivity of 6 W/(m·K)), and clamps were used ensure that all surfaces were in close contact. The loading power of the heating block was adjusted by adjusting the DC power supply so that the setting heat source power (hereinafter referred to as the heating power) was varied from 10 to 100 W in 10 W increments after removing heat losses. Two heating blocks with different heat input areas were used in sequence; the areas were $A_{h1} = 10$ mm × 10 mm and $A_{h2} = 20$ mm × 20 mm. Cooling water at temperatures of 20 °C and 40 °C was passed into the water-cooling plate. The volume flow rate of the cooling water was 0.3 L/min. The accuracy of the temperature control of the cooling-water inlet of the cooling-water circulation system was ±0.01 °C. In the experimental test, when the heat input of a certain power reaches equilibrium (the temperature change within 30 s is <0.5 °C), the heat source power is adjusted for the next measurement.

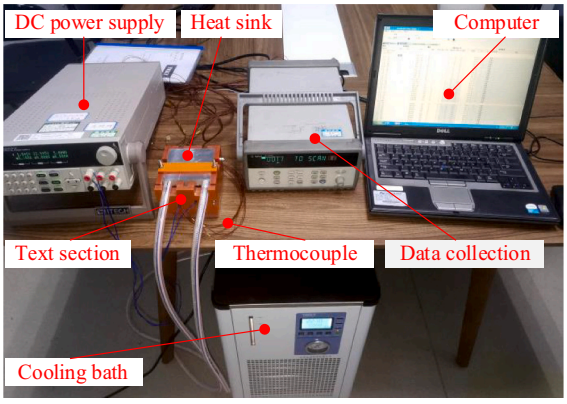

Fig. 8. Field diagram of the heat transfer performance test system of the Vapour Chamber.

The heating block temperature T_h is calculated as:

$$T_h = T_{14} \tag{5}$$

The condensing surface average temperature of the VC are calculated as:

$$T_c = \frac{1}{9}\sum_{i=1}^{9} T_i \tag{6}$$

In a steady state, the maximum temperature difference on the condensing surface ($\Delta T_{C\ max}$) is greater than the maximum temperature difference on the evaporation surface, and $\Delta T_{C\ max}$ is thus used as the

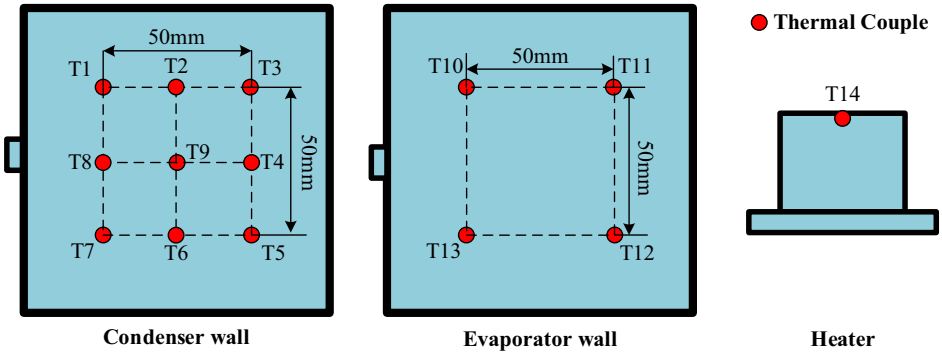

Fig. 7. Schematic diagram of the installation position of the thermocouple.

evaluation parameter of the temperature uniformity of the VC.

$$\Delta T_{Cmax} = max(T_1 \sim T_9) - min(T_1 \sim T_9) \tag{7}$$

The heat transfer resistance R_{VC} is calculated as:

$$R_{VC} = \frac{T_h - T_c}{P} \tag{8}$$

where P is the actual heating power of the heat block.

4.2. Uncertainty analysis

The measurement uncertainty is related to the heating block and the temperature acquisition module. In the heating module, the accuracy of the DC power supply current is 0.1% and the accuracy of the voltage is 0.05%. In the temperature acquisition module, the accuracy of the temperature measurement by the thermocouple is 0.2 °C and the data acquisition resolution is 0.02 °C. The measurement error of each datum in the experiment can be calculated using the formula of Kline and McClintock [31] and Holman [32]:

$$\frac{E(y)}{y} = \frac{\sqrt{\sum_{i=1}^{n}\left(\frac{\partial y}{\partial x_i}Ex_i\right)^2}}{y} \tag{9}$$

where y is the given function of the independent variable x_i, $E(y)$ is the measurement error, and $E\,x_i$ is the maximum measurement error of the independent variable.

The relative measurement uncertainty of the heating power is calculated as 0.2%. When the heating power is >10 W, the maximum relative measurement error of the thermal resistance is 3.36%–10.15%. Uncertainty is estimated on the basis of the 95% confidence interval.

5. Results and discussion

5.1. Effect of the cooling-water temperature

In the test of the heat transfer performance, deionized water having a temperature of 20 or 40 °C was used as the cooling water to determine the effect of the cooling-water temperature on the heat transfer performance of the VCs. Fig. 9. shows the temperature distribution of each temperature measurement point of the AMVC when the cold plate was fed with cooling water at 20 and 40 °C for different areas of the heat source and different heating powers. We see that the temperature distribution of the AMVC changes greatly with the change in the cooling-water temperature. The temperature fluctuation of each temperature measurement point increases with the increase of heat source power. Among the thermocouples, T9 recorded the highest temperature because it was located at the centre of the condensation surface of the AMVC near the heating block. The temperatures recorded by T1, T3, T5, and T7 were lower than the temperatures recorded by the other thermocouples because these four thermocouples were located at the four corners of the condensing surface of the VC, these locations were farthest from the heat source. The temperatures recorded by thermocouples T10–T13 were similar because the four thermocouples were located on the evaporation surface of the VC at the same distance from the heat source. Fig. 10. shows the maximum temperature difference $\Delta T_{C\,max}$ on the AMVC condensing surface when the cooling-water temperature was 20 and 40 °C. We see that throughout the power range of the heat source, $\Delta T_{C\,max}$ of the AMVC condensing surface at T_w = 20 °C was greater than $\Delta T_{C\,max}$ of the condensing surface at T_w = 40 °C, and greater power of the heat source resulted in a greater temperature difference.

For different areas of the heat source, the trends of the temperature change in the AMVC test points were similar, but the temperature fluctuation at T_w = 40 °C was smaller than that at T_w = 20 °C. The main reason for this result is that an increase in the temperature of the cooling water increases the temperature of the VC and decreases the viscosity and flow resistance of the liquid working fluid inside the VC. [36] At the same time, the liquid circulation speed and vapour thermal conductivity increase, the heat transfer rate of the VC increases; the temperature difference between the heating block and evaporator surface decreases. Therefore, as the temperature of the cooling water increases, the temperature difference between the evaporator surface and condenser surface decreases, and the temperature uniformity of the VC improves. However, the surface temperature of the heating block increases with the water temperature, which is not conducive to the control of the heat source temperature. Therefore, in practical applications, it is necessary to select an appropriate cooling-water temperature to improve the heat transfer performance of the VC while maintaining a lower heat source temperature.

The phase change heat transfer cycle within the vapour chamber runs normally when the heat source power is less than the heat transfer limit power. Currently, the temperature of the temperature measurement points on the cooling surface of the vapour chamber and the temperature differential between the temperature measurement points are progressively increasing as the heat source power increases. At this level, the temperature difference between each measurement point is

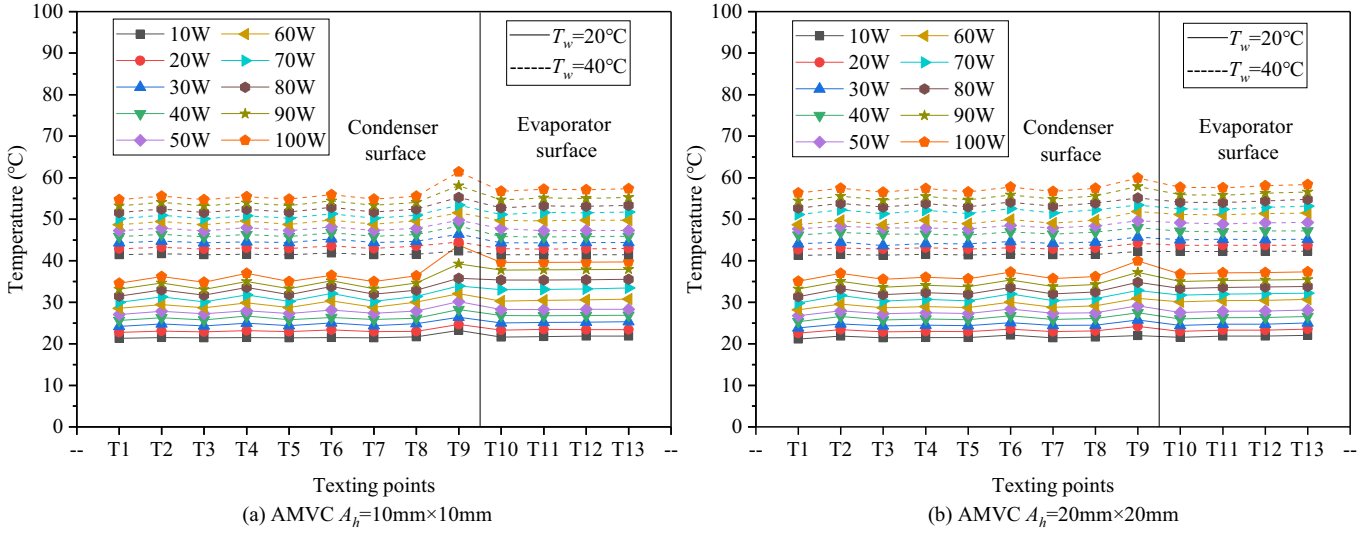

Fig. 9. Temperature distribution of the AMVC at different cooling water temperatures.

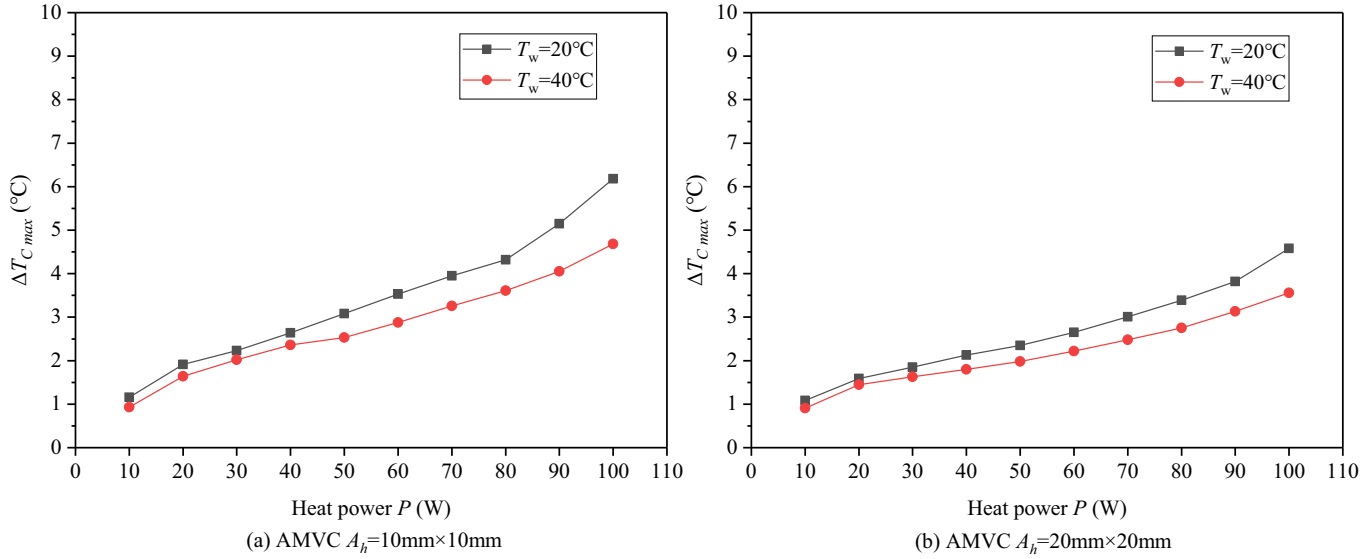

Fig. 10. Maximum temperature difference on the condenser surface of the AMVC at different cooling water temperatures.

tiny, and the temperature uniformity plate has excellent temperature uniformity. When the heat source power exceeds the heat transfer limit power, the evaporation portion of the vapour chamber experiences "partial dry-out." The destruction of the phase change heat transfer cycle within the vapour chamber has a negative impact on the heat diffusion from the high-temperature region in the vapour chamber's center to its surroundings. At this moment, as the heat source power grows, the temperature of the T9 positioned in the center of the condensing surface of the vapour chamber increases fast, as does the temperature difference between the temperature measuring points. During this stage, the temperature homogeneity of the vapour chamber gradually deteriorates.

5.2. Effect of the heating source area

Figs. 11 and 12 compare the maximum temperature difference $\Delta T_{C\,max}$ and thermal resistance R of the AMVC for different heating source areas. We see that throughout the power range, the maximum temperature difference of the AMVC condensation surface when the heat source area was $A_h = 20$ mm × 20 mm is smaller than that when the heat source area $A_h = 10$ mm × 10 mm. When $P = 100$ W and $A_h = 20$ mm × 20 mm, the maximum temperature difference of the AMVC condensing surface was reduced by 1.61 °C ($T_w = 20$ °C) and 1.12 °C ($T_w = 40$ °C) relative to that for $A_h = 10$ mm × 10 mm. Therefore, under the same conditions, increasing the area of the heat source can improve the temperature uniformity of the VC. Fig. 11 shows that throughout the power range, when the heat source area was $A_h = 20$ mm × 20 mm, the thermal resistance of AMVC was smaller than that when the heat source area was $A_h = 10$ mm × 10 mm. Since the evaporating heat flux decreases with increasing heating area, the evaporator resistance decreases and the vapour temperature generated vapour temperature decreases. As a result, T9 decreases and more uniform condenser temperatures manifest. The increasing thermal resistance with a decrease in the heat source's surface area is also a result of the conductivity spreading laterally [35]. When the surface area of the heat source is small, heat concentration forms on the evaporator. At this point, nucleate boiling will begin, causing the working fluid to rapidly evaporate and produce bubbles in the evaporation section. The bubbles will impede the horizontal flow of the working fluid in the evaporation wick, destroying the

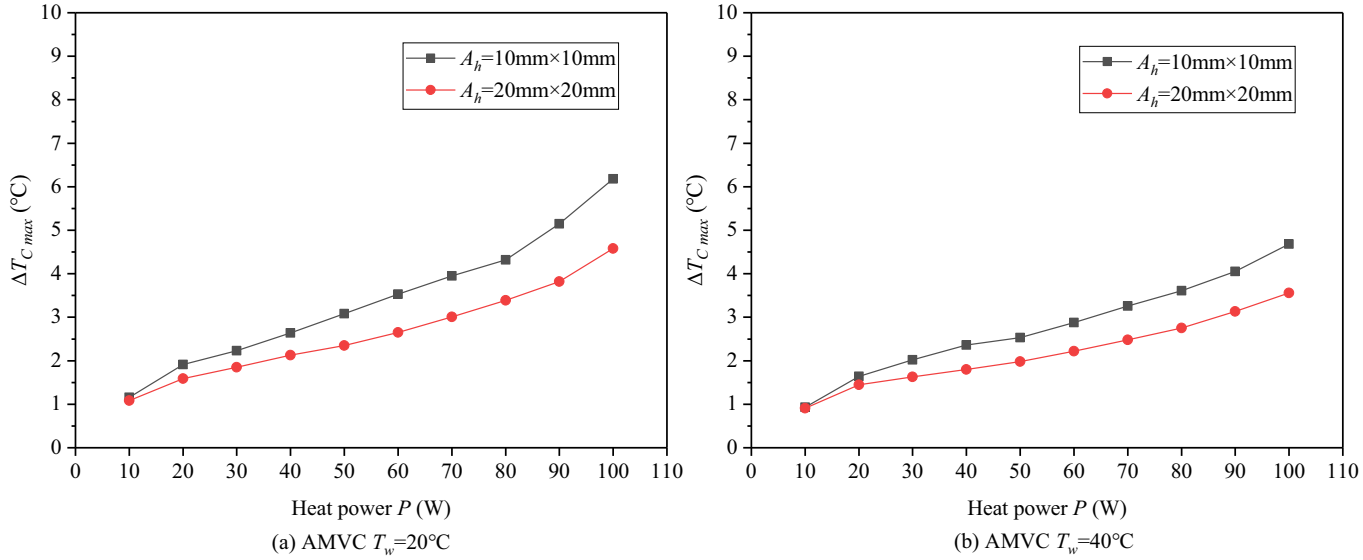

Fig. 11. Maximum temperature difference on the condensing surface of AMVC by the different areas of the heating source.

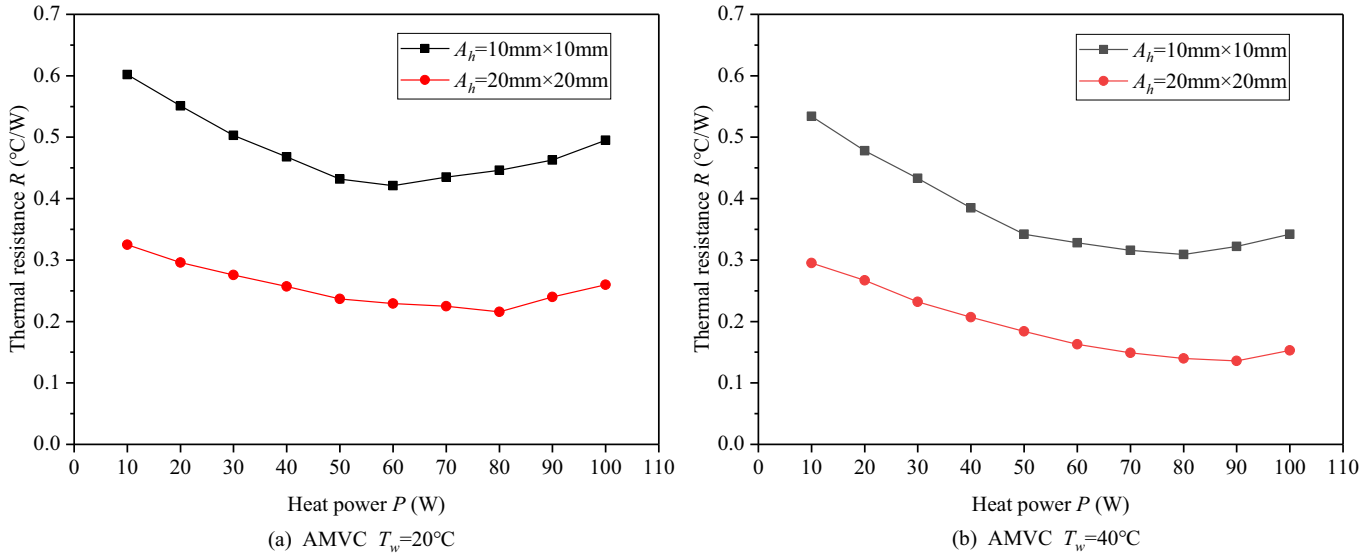

Fig. 12. Thermal resistance of AMVC by the different areas of the heating source.

phase change heat transfer cycle of the working fluid within the vapour chamber. Consequently, the lateral diffusion effect occurs when the heat source's surface area is modest. Currently, the phase change cycle of the working fluid within the vapour chamber is decelerating, and conduction is becoming the primary mode of heat transfer; consequently, the thermal resistance is increasing. When a large-area heat source is employed, the phase change cycle of the fluid within the vapour chamber is less influenced, resulting in the vapour chamber exhibiting improved temperature uniformity and decreased heat transfer resistance.

5.3. Effect of the hybrid-pore wick structure

Figs. 13 and 14 respectively show $\Delta T_{C\,max}$ and R curves of the AMVC and AMVC-H when A_h = 20 mm × 20 mm. It is seen from Fig. 12 that $\Delta T_{C\,max}$ of the AMVC-H at different cooling-water temperatures was smaller than that of the AMVC. When $P \leq 50$ W, $\Delta T_{C\,max}$ was similar for the AMVC-H and AMVC condensing surfaces. When $P \geq 50$ W, the growth rate of $\Delta T_{C\,max}$ on the AMVC increased. At this time, the growth rate of $\Delta T_{C\,max}$ of the AMVC-H decreased, and the difference in $\Delta T_{C\,max}$ between the AMVC-H and the AMVC gradually increased. The AMVC-H thus has better temperature uniformity under high heat power. It is seen from Fig. 13 that the thermal resistance of the AMVC-H was lower than that of the AMVC throughout the power range. When P = 100 W, the thermal resistance of the AMVC-H at cooling-water temperatures of T_w = 20 °C and 40 °C was 0.158 °C/W and 0.077 °C/W, respectively. Relative to the AMVC under the same power, the thermal resistance was reduced by 39.2% and 49.6%.

The AMVC-H has better temperature uniformity and better heat transfer performance than the AMVC, and the effect is more obvious in the case of higher heat power. This is because when the input power of the heat source is low, the evaporation intensity of the liquid working medium inside the VC is weak, and there is enough liquid working fluid on the evaporation surface to complete the phase-change heat-transfer cycle. Therefore, the AMVC and AMVC-H have similar heat transfer capabilities at low heat power. When the input power increases, the

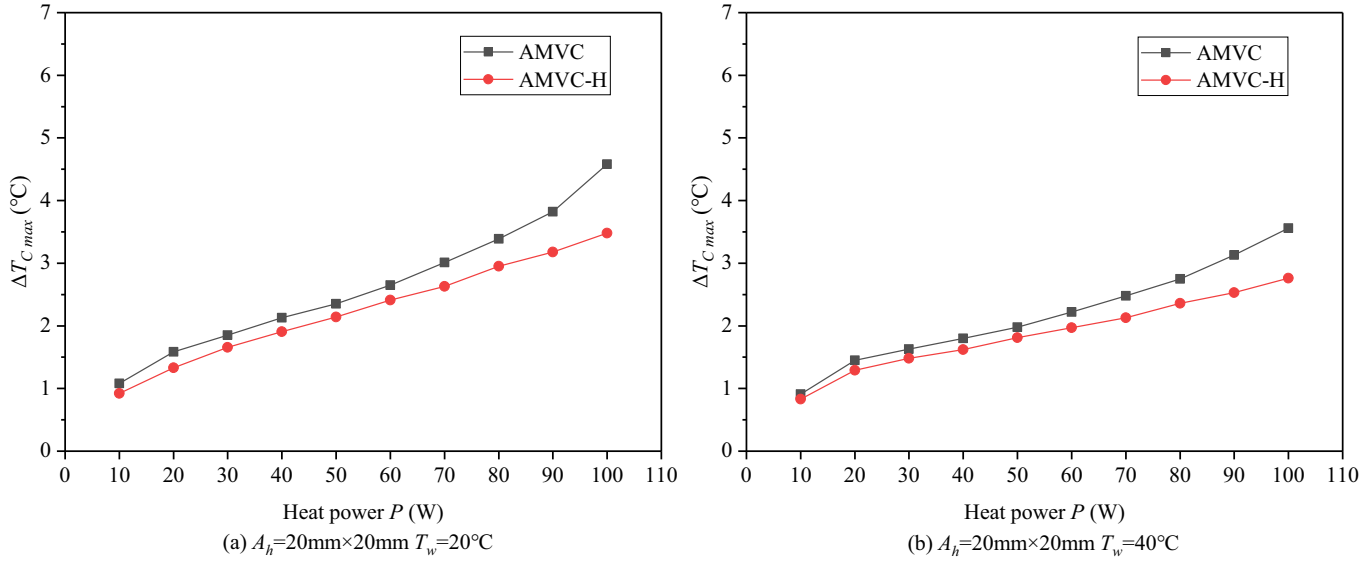

Fig. 13. The maximum temperature difference of the VCs condensation surface at different cooling water temperatures, when the heat source area A_h = 20 mm × 20 mm.

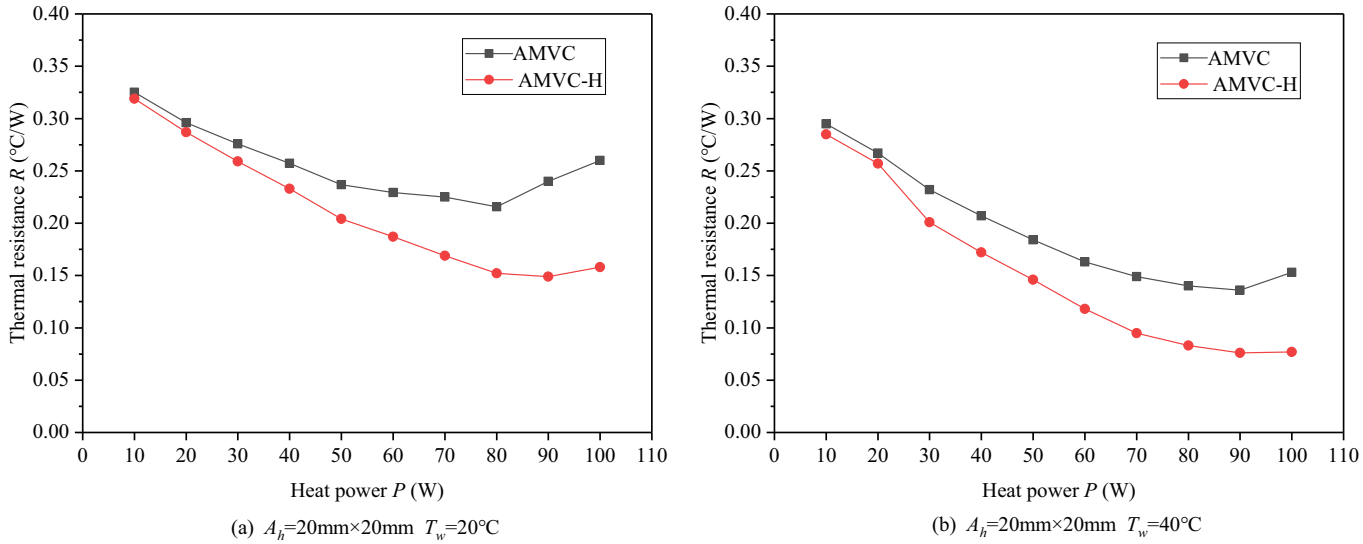

Fig. 14. Thermal resistance of the VCs under different cooling water temperatures when the area of the heat source A_h = 20 mm × 20 mm.

liquid working fluid in the evaporation wick quickly absorbs heat and evaporates, the capillary pressure of the large-pore evaporation wick of the AMVC cannot deliver enough liquid working fluid to the evaporation area, and, as a result, "partial dry-out" occurs in the evaporator and the temperature difference of the AMVC condensing surface increases rapidly. In the AMVC-H, a hybrid-pore wick was prepared by printing a small-pore frame structure at the centre of the evaporator wick. A higher capillary pressure, provided by the small-pore porous area and combined with the excellent permeability of the surrounding large-pore porous structure, could quickly transport more working fluid to the evaporation part for heat exchange. [14] Thus, the AMVC-H thus had better heat transfer performance in the case of higher heat power. Meanwhile, the hybrid wick with a smaller porosity, it was expected to have a higher thermal conductivity. Consequently, due to the lower evaporator resistance, the vapour temperature generated from the evaporator was reduced, and, in turn, T9 was decreased. Additionally, it led to better temperature uniformity and heat transfer performance.

5.4. Thermal resistance comparison

The minimum thermal resistance is given in Table 5 to compare the proposed solution with several VC heat sinks reported in previous studies, where the size, heat load, and wick type also given because these parameters affect the thermal resistance. We see that the VCs with different structure sizes and the traditionally manufactured wick structure have different maximum heat transfers and heat transfer resistances.

Liu et al. [12] developed a circular VC with a vein-like fractal network wick. In their work, the thermal resistance of the VC decreased with increasing the heat flux, and a minimum thermal resistance of 0.06 °C /W was obtained at 140 W heat power. Huang et al. [34] fabricated and tested a series of VCs with sintered copper powder wicks, which had an overall VC thickness of 3 mm, and at heat power of 78 W the minimum thermal resistance was 0.24 °C /W. Chen et al. [10] studied the effects of liquid filling rate and leakage on the cooling performance of flat plate heat pipes. The results showed that the liquid filling ratio of 25% had the best thermal performance. Moreover, the corresponding maximum heat transport capability, minimum thermal resistance, and maximum effective thermal conductivity were approximately 47 W, 0.254 K/W, and 3150 W/m K, respectively. In contrast, improper vacuum and leakage could significantly decrease the maximum thermal conductivity to about 200–306 W/m K and 164 W/m K, respectively. Paiva et al. [33] presented a theoretical and experimental analysis of a copper mini heat pipe, the results showed that the maximum heat transfer and minimum heat transfer thermal resistance of the heat pipe were 45 W and 0.4 W/°C, respectively. Huang et al. [13] fabricated and studied a series of cost-effective sintered copper mesh Ultra-thin vapour chamber (UTVC) (total thickness: 1.26–1.77 mm). Moreover, they experimentally investigated the effects of coarse mesh and wire diameter, fine mesh, inclination angle and cooling –water temperature on the heat transfer performance of UTVC. The results showed that SP3 (1.53 mm) could dissipate 50 W horizontally, and the thermal resistance was 0.197 °C/W, which being about 4.4 times lower than that of a 1.5 mm copper plate. Wong et al. [11] conducted heat transfer performance tests on new vapour chambers with different working fluids. They found that the lowest minimum vapour chamber resistances were obtained for water, and the thermal resistance was 0.14 °C/W under a heat flux of 120 W.

Table 5
Thermal performances of various Vapour Chambers.

Reference	t (mm)	Wick	P_{max} (W)	R_{min}(°C/W)
Liu et al. [12]	4.8	Vein-shaped fractal wick	140	0.06
Huang et al. [34]	3	Sintered-copper powder	78	0.24
Chen et al. [10]	2.5	Grooves- aluminum	47	0.254
Paiva et al. [33]	2	Grooves	45	≈0.4
Huang et al. [13]	1.5	Sintered -copper mesh	50	0.197
Wong et al. [11]	1.5	Grooves-copper	120	0.14
AMVC	2.97	3D printed wick	100	0.154
AMVC-H	2.97	Hybrid-3D printed wick	100	0.077

In this work, the heat transfer performance of two types of VCs (AMVC、AMVC-H) with different 3D printed wick structures were experimentally studied. In this regard, different cooling conditions were considered, including the cooling water temperature, heating power and heating source area. The two 3D printing wick structures used different unit structures in the evaporation part, i.e., the condensation part and the porous structure support column. Moreover, the 3D hybrid-pore wick was prepared by printing a small-pore-area structure in the center of the evaporation part wick. As shown in Fig. 15, for the heating power of 80 W, the thermal resistance of AMVC and AMVC-H was reduced by 41.67% and 65.41%, respectively, compared with the previous research results [33], indicating that the 3D printing wick structure was beneficial for improving the heat transfer performance of VCs. The reason is that the 3D printing wick structure adopted different unit structures at different positions, and the porous structure column was

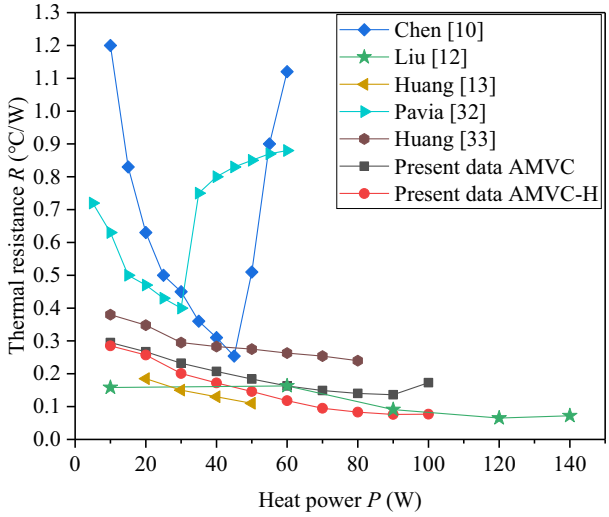

Fig. 15. Comparison of the thermal resistance between the present data and those reported in earlier publications.

printed between the evaporating part wick and the condensing part wick. This design enabled the 3D printing wick to enhance the evaporation of the working liquid, while accelerating the circulation of the working liquid inside the vapour chamber. Therefore, the VCs with 3D printed wick had better temperature uniformity and lower thermal resistance to heat transfer. In the AMVC-H, a hybrid-pore wick is formed by printing a small-pore frame structure at the centre of the evaporator wick. The small-pore porous area provided higher capillary pressure, which, along with the excellent permeability of the surrounding large-pore porous structure, quickly transported more liquid working fluid to the evaporation part for heat exchange. Thus, the AMVC-H had better temperature uniformity and better heat transfer performance in the case of higher heat power.

Compared to conventional manufacturing methods, additive manufacturing has many advantages in wick manufacturing. First, AM enables the precise control of the structure type and cell size of the porous structure at each place along the wick by arranging the laser scanning path and adjusting the printing settings. Thus, it is possible to produce high-performance wicks that combine the benefits of several porosity architectures. Such production is unattainable using conventional procedures. Second, each position of the wick obtained by additive manufacturing has its own specific type and size of porous structure, which provides a foundation for deriving the heat transfer model of the entire vapour chamber by analyzing the phase change cycle process of the working fluid within the complex wick structure. Thirdly, the integrated production feature of 3D printing substantially simplifies and increases the efficiency of the manufacturing process. The characteristics of free stacking and shaping of materials throughout the manufacturing and molding processes indicate that AM has promising application possibilities in the production of special-shaped wicks, the overall printing and production of VCs, and the integrated production of VCs.

6. Conclusion

This paper used 3D-printed wicks in vapour chamber fabrication for the first time. Two types of VC with integrated 3D printed wicks were developed to demonstrate the feasibility of adopting metallic AM for VC manufacturing. The effects of the cooling-water temperature, heat source area, and mixed wick structure on the thermal performance of the VC were studied by conducting water-cooling experiments. The main conclusions are summarized as follows.

(1) Using 3D printed wicks in vapour chambers is a viable solution. The 3D printed-wick VC adopting an integrated porous structure column can achieve good heat conduction within a certain power range. When $A_h = 20$ mm $\times$ 20 mm and $T_w = 40$ °C, the AMVC and AMVC-H could withstand a thermal load of 100 W.

(2) Similar to other vapour chambers with traditionally fabricated wicks, the temperature of the cooling water and the heat source area significantly affected the heat transfer performance of the 3D printed-wick VC. When $T_w = 40$ °C, the VC has better temperature uniformity and lower thermal resistance. Increasing the area of the heat source can reduce the diffusion resistance of the heat transfer to the surroundings in the VC, thereby improving the heat transfer performance.

(3) The 3D printed hybrid-pore wick can improve the heat transfer performance of the VC, and the performance improvement is more obvious under the condition of higher heating power. When $P = 100$ W, the thermal resistance of the AMVC-H is 0.158 and 0.077 °C/W at cooling-water temperatures $T_w = 20$ °C and 40 °C, respectively. Compared with the thermal resistance of the AMVC under the same power, the thermal resistance is reduced by 39.2% and 49.6%.

(4) Additive Manufacturing allows the precise control of the shape and cell size of the porous structure of each part of the wick, such that a high-performance wick structure that combines large capillary pressure and high permeability can be manufactured. The heat transfer performance of the VC can thus be further improved. AM also provides new ideas for the overall printing and integrated manufacturing of VCs.

CRediT authorship contribution statement

Xu Meng: Data curation, Writing – original draft, Validation. **Shujie Tan:** Software. **Zhipeng Yuan:** Investigation. **Yicha Zhang:** Writing – review & editing. **Liheng Chen:** Conceptualization, Methodology.

Declaration of Competing Interest

The authors declare that there is no conflict of interest.

Data availability

The authors do not have permission to share data.

Acknowledgement

This research was supported by the Fengyun-3 satellite project funding, and the technical support was provided by the Nanjing Profeta Intelligent Technology Co, Ltd.

References

[1] D.A. Reay, P.A. Kew, R.J. McGlen, Heat Pipes, sixth ed., Elsevier, Oxford, 2014.
[2] Y. Tang, L. Lin, S. Zhang, J. Zeng, K. Tang, G. Chen, W. Yuan, Thermal management of high-power LEDs based on integrated heat sink with vapour chamber, Energy Convers. Manag. 151 (2017) 1–10.
[3] J.-C. Wang, W.-J. Chen, Vapour chamber in high-end VGA card, in: 2011 6th International Microsystems, Packaging, Assembly and Circuits Technology Conference (IMPACT), IEEE, 2011, pp. 393–396.
[4] P. Naphon, S. Wongwises, S. Wiriyasart, Application of two-phase vapour chamber technique for hard disk drive cooling of PCs, Int. Comm. Heat and Mass Transf. 40 (2013) 32–35.
[5] Q. Cai, B.-c. Chen, C. Tsai, Design, development and tests of high-performance silicon vapour chamber, J. Micromech. Microeng. 22 (2012), 035009.
[6] T. Vaneker, A. Bernard, G. Moroni, I. Gibson, Y. Zhang, Design for additive manufacturing: framework and methodology, CIRP Ann. 69 (2020) 578–599.
[7] W. Wang, C. Zheng, F. Tang, Y. Zhang, A practical redesign method for functional additive manufacturing, Procedia. CIRP 100 (2021) 566–580.
[8] Y. Zhang, S. Tan, L. Ding, A. Bernard, A toolpath-based layer construction method for designing & printing porous structure, CIRP Ann. Manuf. Technol. 70 (2021) 123–126.

[9] A. Faghri, Heat Pipe Science and Technology, Global Digital Press, 1995.
[10] J.-S. Chen, J.-H. Chou, Cooling performance of flat plate heat pipes with different liquid filling ratios, Int. J. Heat Mass Transf. 77 (2014) 874–882.
[11] S.-C. Wong, S.-F. Huang, K.-C. Hsieh, Performance tests on a novel vapour chamber, Appl. Therm. Eng. 31 (2011) 1757–1762.
[12] W. Liu, Y. Peng, T. Luo, Y. Luo, K. Huang, The performance of the vapour chamber based on the plant leaf, Int. J. Heat Mass Transf. 98 (2016) 746–757.
[13] G. Huang, W. Liu, Y. Luo, Y. Li, H. Chen, Fabrication and thermal performance of mesh-type ultra-thin vapour chambers, Appl. Therm. Eng. 162 (2019), 114263.
[14] F. Lefèvre, J.-B. Conrardy, M. Raynaud, J. Bonjour, Experimental investigations of flat plate heat pipes with screen meshes or grooves covered with screen meshes as capillary structure, Appl. Therm. Eng. 37 (2012) 95–102.
[15] C. Oshman, Q. Li, L.-A. Liew, R. Yang, V.M. Bright, Y. Lee, Flat flexible polymer heat pipes, J. Micromech. Microeng. 23 (2012), 015001.
[16] Y.-T. Chen, S.-W. Kang, Y.-H. Hung, C.-H. Huang, K.-C. Chen, Feasibility study of an aluminum vapour chamber with radial grooved and sintered powders wick structures, Appl. Therm. Eng. 51 (2013) 864–880.
[17] Y. Tang, D. Yuan, L. Lu, Z. Wang, A multi-artery vapour chamber and its performance, Appl. Therm. Eng. 60 (2013) 15–23.
[18] M. Kim, M. Kaviany, Multi-artery heat-pipe spreader: monolayer-wick receding meniscus transitions and optimal performance, Int. J. Heat Mass Transf. 112 (2017) 343–353.
[19] B. He, M. Wei, S. Somasundaram, C.S. Tan, E.N. Wang, Experiments on the ultrathin silicon vapour chamber for enhanced heat transfer performance, in: 2016 15th IEEE Intersociety Conference on Thermal and Thermomechanical Phenomena in Electronic Systems (ITherm), IEEE, 2016, pp. 569–573.
[21] S.-C. Wong, W.-S. Liao, Visualization experiments on flat-plate heat pipes with composite mesh-groove wick at different tilt angles, Int. J. Heat Mass Transf. 123 (2018) 839–847.
[22] B. Yan, C. Wang, L. Li, The technology of micro heat pipe cooled reactor: a review, Ann. Nucl. Energy 135 (2020), 106948.
[23] A. Faghri, Review and advances in heat pipe science and technology, J. Heat Transf. 134 (2012).
[24] N. Lebaal, Y. Zhang, F. Demoly, S. Roth, S. Gomes, A. Bernard, Optimised lattice structure configuration for additive manufacturing, CIRP Ann. 68 (2019) 117–120.
[25] Y. Zhang, Z. Wang, Y. Zhang, S. Gomes, A. Bernard, Bio-inspired generative design for support structure generation and optimization in additive manufacturing (AM), CIRP Ann. 69 (2020) 117–120.
[26] X. Lu, P.J. Thomas, Y. Zhang, H. Liao, S. Gomes, J.O. Hellevang, Characterization of optical fibers directly embedded on metal using a particle spray-based method, IEEE Sensors J. 20 (2020) 6414–6421.
[27] Y. Zhang, L.H. Chen, X. Meng, et al., Performance characterization and printing parameter modelling of selective laser melting printed capillary wicks, Rapid Prototyp. J. 28 (2021) 1558–1572.
[28] S. Luo, Q. Wang, R. Ye, C.S. Ramachandran, Effects of electrolyte concentration on the microstructure and properties of plasma electrolytic oxidation coatings on Ti-6Al-4V alloy, Surf. Coat. Technol. 375 (2019) 864–876.
[29] M.C. Tsai, S.W. Kang, K.V. de Paiva, Experimental studies of thermal resistance in a vapour chamber heat spreader - ScienceDirect, Appl. Therm. Eng. 56 (2013) 38–44.
[30] S. Maruyama, in: Translated by S.X. W ang, X.R. Zhang, et al. (Eds.), Heat Transfer, seventh ed, Peking University Press, Beijing, 2011.
[31] S.J. Kline, Describing uncertainty in single-sample experiments, Mech. Eng. 75 (1953).
[32] J.P. Holman, Experimental Methods for Engineers, 2012.
[33] K.V.D. Paiva, M.B.H. Mantelli, L.K. Slongo, Thermal behavior analysis of wire mini heat pipe, J. Heat Transf. 133 (2011), 121502.
[34] D. Huang, L. Jia, H. Wu, O. Aaker, Experimental investigation on the vapour chambers with sintered copper powder wick, J. Therm. Sci. 30 (2021) 1938–1950.
[35] J.-Y. Chang, R.S. Prasher, S. Prstic, P. Cheng, H. Ma, Evaporative thermal performance of vapour chambers under nonuniform heating conditions, J. Heat Transf. 130 (2008).
[36] Y. Li, W. Zhou, Z. Li, Z. Chen, Y. Gan, Experimental analysis of thin vapour chamber with composite wick structure under different cooling conditions, Appl. Therm. Eng. 156 (2019) 471–484.

Parameter description

Nomenclature

Symbols:
t: thickness (mm)
L: length (mm)
W: width (mm)
OD: outer diameter (mm)
AM: Additive Manufacturing
d: average diameter (μm)
M: quality (g)
V: volume
K: Wick permeability (μm2)
P: heat load (W)
R: thermal resistance (K/W)
T: temperature (°C)
x: distance (mm)
C: integral constant
r_{eff}: effective capillary radius (μm)
AMVC: Single-pore 3D printed wick vapour chamber
AMVC-H: hybrid-pore 3D printed wick vapour chamber
Greek symbols:
ε: porosity (%)
Δ: difference
η: filling ratio (%)
Subscripts:
wi: wick
por: pore
wl: working fluid
vc: vapour chamber
h: heating block
e: evaporator surface
c: condenser surface
w: Cooling water
dw: deionized water